



Synthesis and characterization of Ti–Mn and Ti–Fe codoped $\text{Li}_3\text{V}_2(\text{PO}_4)_3$ as cathode material for lithium ion batteries

S. Zhang^{a,**}, Q. Wu^a, C. Deng^{b,*}, F.L. Liu^a, M. Zhang^a, F.L. Meng^a, H. Gao^a

^a College of Material Science and Chemical Engineering, Harbin Engineering University, Harbin 150001, Heilongjiang, China

^b Key Laboratory for Photonic and Electronic Bandgap Materials, Ministry of Education; College of Chemistry and Chemical Engineering, Harbin Normal University, Harbin 150025, Heilongjiang, China

HIGHLIGHTS

- ▶ Ti–Mn and Ti–Fe codoped $\text{Li}_3\text{V}_2(\text{PO}_4)_3$ samples were prepared by a sol–gel method.
- ▶ Single phase $\text{Li}_3\text{V}_{2-2x}\text{Ti}_x\text{Mn}_x(\text{PO}_4)_3$ and $\text{Li}_3\text{V}_{2-2x}\text{Ti}_x\text{Fe}_x(\text{PO}_4)_3$ were detected as $x \leq 0.05$.
- ▶ $\text{Li}_3\text{V}_{1.9}\text{Ti}_{0.05}\text{Fe}_{0.05}(\text{PO}_4)_3$ has improved electrochemical performance than undoped one.

ARTICLE INFO

Article history:

Received 23 February 2012

Received in revised form

30 May 2012

Accepted 1 June 2012

Available online 26 June 2012

Keywords:

Lithium ion battery

Lithium vanadium phosphate

Codoping

Manganese

Iron

ABSTRACT

Ti–Mn and Ti–Fe codoped $\text{Li}_3\text{V}_2(\text{PO}_4)_3$ samples, i.e. $\text{Li}_3\text{V}_{2-2x}\text{Ti}_x\text{Mn}_x(\text{PO}_4)_3$ and $\text{Li}_3\text{V}_{2-2x}\text{Ti}_x\text{Fe}_x(\text{PO}_4)_3$ ($x = 0, 0.05, 0.1, 0.15, 0.2$ and 0.25), are prepared by a sol–gel method. $\text{Li}_3\text{V}_{2-2x}\text{Ti}_x\text{Mn}_x(\text{PO}_4)_3$ and $\text{Li}_3\text{V}_{2-2x}\text{Ti}_x\text{Fe}_x(\text{PO}_4)_3$ are phase-pure when x is not higher than 0.05. LiMnPO_4 and LiFePO_4 begin to form as impurity phases in $\text{Li}_3\text{V}_{2-2x}\text{Ti}_x\text{Mn}_x(\text{PO}_4)_3$ and $\text{Li}_3\text{V}_{2-2x}\text{Ti}_x\text{Fe}_x(\text{PO}_4)_3$, respectively, when x is equal to 0.1. And another impurity of $\text{Mn}_2\text{P}_2\text{O}_7$ appears in $\text{Li}_3\text{V}_{2-2x}\text{Ti}_x\text{Mn}_x(\text{PO}_4)_3$ when x is equal to 0.2. All these impurities increase with increasing x . XPS analyses indicate that the oxidation states of Ti, Mn and Fe are +4, +2 and +2 respectively. The first charge/discharge capacities of both $\text{Li}_3\text{V}_{2-2x}\text{Ti}_x\text{Mn}_x(\text{PO}_4)_3$ and $\text{Li}_3\text{V}_{2-2x}\text{Ti}_x\text{Fe}_x(\text{PO}_4)_3$ at 0.2 C decline with an increase of x . Both the high-rate discharge capability and long term cycling performance of $\text{Li}_3\text{V}_{1.9}\text{Ti}_{0.05}\text{Fe}_{0.05}(\text{PO}_4)_3$ are much better than those of $\text{Li}_3\text{V}_2(\text{PO}_4)_3$, which can be attributed to the smaller particle size, larger lattice parameters and better structural stability induced by Ti and Fe codoping. However, the electrochemical performance of $\text{Li}_3\text{V}_{1.9}\text{Ti}_{0.05}\text{Mn}_{0.05}(\text{PO}_4)_3$ is worse than that of $\text{Li}_3\text{V}_2(\text{PO}_4)_3$, which is due to the structural instability induced by the incorporation of Mn.

© 2012 Elsevier B.V. All rights reserved.

1. Introduction

Battery-powered electric vehicles are environmentally friendly because they don't pollute. Lithium ion batteries have high energy and power density, thus they are considered as one of the best choices for electric vehicles [1–4]. Lithium vanadium phosphate, i.e. $\text{Li}_3\text{V}_2(\text{PO}_4)_3$, is a promising cathode materials for lithium ion batteries because it has large capacity and high thermal stability [5–7]. Two lithium ions can be reversibly extracted/inserted if only the $\text{V}^{3+}/\text{V}^{4+}$ redox couple is utilized. All the three lithium ions can

be completely extracted if the cutoff potential of charge is set to 4.8 V, which results in a theoretical capacity of 197 mAh g^{-1} .

Despite its many advantages over other cathode materials, $\text{Li}_3\text{V}_2(\text{PO}_4)_3$ does suffer from low electronic and ionic conductivity. Cation doping is an effective way to solve this problem. Cations such as Al^{3+} [8], Fe^{3+} [9], Cr^{3+} [10], Mg^{2+} [11], Co^{2+} [12] and Ti^{4+} [13] have been employed to dope $\text{Li}_3\text{V}_2(\text{PO}_4)_3$. Although some improvements are realized by cation doping, the electrochemical performance is far from ideal [8–15]. Therefore, it is necessary to explore new doping strategies.

Recently, Ti–Mg codoping has been applied to improve the electrochemical performance of $\text{Li}_3\text{V}_2(\text{PO}_4)_3$ [16,17]. The oxidation states of Ti and Mg are +4 and +2, respectively; hence this doping strategy has the advantage of charge neutrality if the amounts of Ti and Mg are equal. Although a low amount of doping can improve the rate capability and cycle stability, it lowers the discharge

* Corresponding author. Tel.: +86 451 88060570.

** Corresponding author. Tel.: +86 451 82589186.

E-mail addresses: senzhang@hrbeu.edu.cn (S. Zhang), chaodeng2008@yahoo.cn (C. Deng).

capacity at low current density because Ti and Mg are electrochemically inert [17]. Divalent cations such as Fe^{2+} and Mn^{2+} are electrochemically active. Therefore, it is favorable to replace the electrochemically inert Mg^{2+} with the electrochemically active Fe^{2+} or Mn^{2+} .

In this study, Ti–Mn and Ti–Fe codoped $\text{Li}_3\text{V}_2(\text{PO}_4)_3$, i.e. $\text{Li}_3\text{V}_{2-2x}\text{Ti}_x\text{Mn}_x(\text{PO}_4)_3$ and $\text{Li}_3\text{V}_{2-2x}\text{Ti}_x\text{Fe}_x(\text{PO}_4)_3$ ($x = 0, 0.05, 0.10, 0.15, 0.20, 0.25$), are prepared by a sol–gel method. Their physical and electrochemical properties are characterized in detail.

2. Experimental

2.1. Synthesis of $\text{Li}_3\text{V}_{2-2x}\text{Ti}_x\text{Mn}_x(\text{PO}_4)_3$ and $\text{Li}_3\text{V}_{2-2x}\text{Ti}_x\text{Fe}_x(\text{PO}_4)_3$

The $\text{Li}_3\text{V}_{2-2x}\text{Ti}_x\text{Mn}_x(\text{PO}_4)_3$ and $\text{Li}_3\text{V}_{2-2x}\text{Ti}_x\text{Fe}_x(\text{PO}_4)_3$ ($x = 0, 0.05, 0.1, 0.15, 0.20, 0.25$) samples were prepared by a sol–gel method. The starting materials were analytically pure $\text{LiOH} \cdot \text{H}_2\text{O}$, NH_4VO_3 , $\text{NH}_4\text{H}_2\text{PO}_4$, TiO_2 , $\text{Mn}(\text{CH}_3\text{COO})_2 \cdot 4\text{H}_2\text{O}$, $\text{FeC}_6\text{H}_5\text{O}_7 \cdot 5\text{H}_2\text{O}$ and $\text{C}_6\text{H}_8\text{O}_7 \cdot \text{H}_2\text{O}$. Stoichiometric amounts of the starting materials were dissolved in distilled water under magnetic stirring. The resulting solution was kept stirring at 80°C until a wet gel was formed. The wet gel was dried at 100°C over night to form a dry gel. The dry gel was ground and heated at 700°C for 8 h in flowing argon.

The $\text{Li}_3\text{V}_2(\text{PO}_4)_3$ sample was mechanically milled to smaller particle size. It was sealed in a stainless-steel container together with zirconia balls inside an argon-filled glove box. The container was fixed on a high-speed planetary mill. The ball-to-powder weight ratio and milling speed are 20:1 and 400 rpm, respectively. The milling was interrupted for 30 min every 1 h and lasted for 6 h. The resulting powder was collected for characterization.

2.2. Measurements

Powder X-ray diffraction (XRD, Bruke D8) employing Cu K α radiation was used to identify the crystalline phase of the materials. The surface morphology was observed with a scanning electron microscope (SEM, HITACHI S-4700). X-ray photoelectron spectroscopy (XPS, Thermo ESCALAB 250) was employed to measure the chemical or electronic state of each element, and Al K α (1486.6 eV) was the photon energy of choice. The carbon content of each sample was measured by using a CHNS Elemental Analyzer (EA, Vario EL III, Elementar).

The coin cell was prepared as described in Ref. [18]. The composite electrode was made from a mixture of the prepared sample, acetylene black, and Polyvinylidene Fluoride (PVdF) in a weight ratio of 80:10:10. Galvanostatic charge–discharge measurements were performed in a potential range of 3.0–4.8 V. EIS measurements were conducted at a fully discharged state using a CHI 660C electrochemical workstation, and the applied frequency range is 100 kHz–0.1 Hz.

3. Results and discussion

3.1. Structural characterization

Fig. 1(a) and (b) shows the XRD patterns of all the $\text{Li}_3\text{V}_{2-2x}\text{Ti}_x\text{Mn}_x(\text{PO}_4)_3$ and $\text{Li}_3\text{V}_{2-2x}\text{Ti}_x\text{Fe}_x(\text{PO}_4)_3$ ($x = 0, 0.05, 0.1, 0.15, 0.20, 0.25$) samples. The XRD pattern of the $\text{Li}_3\text{V}_2(\text{PO}_4)_3$ sample can be indexed on the monoclinic unit cell in space group $P2_1/n$. The XRD patterns of $\text{Li}_3\text{V}_{1.9}\text{Ti}_{0.05}\text{Mn}_{0.05}(\text{PO}_4)_3$ and $\text{Li}_3\text{V}_{1.9}\text{Ti}_{0.05}\text{Fe}_{0.05}(\text{PO}_4)_3$ are similar to that of $\text{Li}_3\text{V}_2(\text{PO}_4)_3$, and no extra reflections are observed. This indicates that Ti and Mn or Ti and Fe enter in to the structure of $\text{Li}_3\text{V}_{1.9}\text{Ti}_{0.05}\text{Mn}_{0.05}(\text{PO}_4)_3$ or $\text{Li}_3\text{V}_{1.9}\text{Ti}_{0.05}\text{Fe}_{0.05}(\text{PO}_4)_3$ rather than form impurities when x is not higher than 0.05. Diffraction peaks of impurities begin to appear in the XRD patterns when x is increased

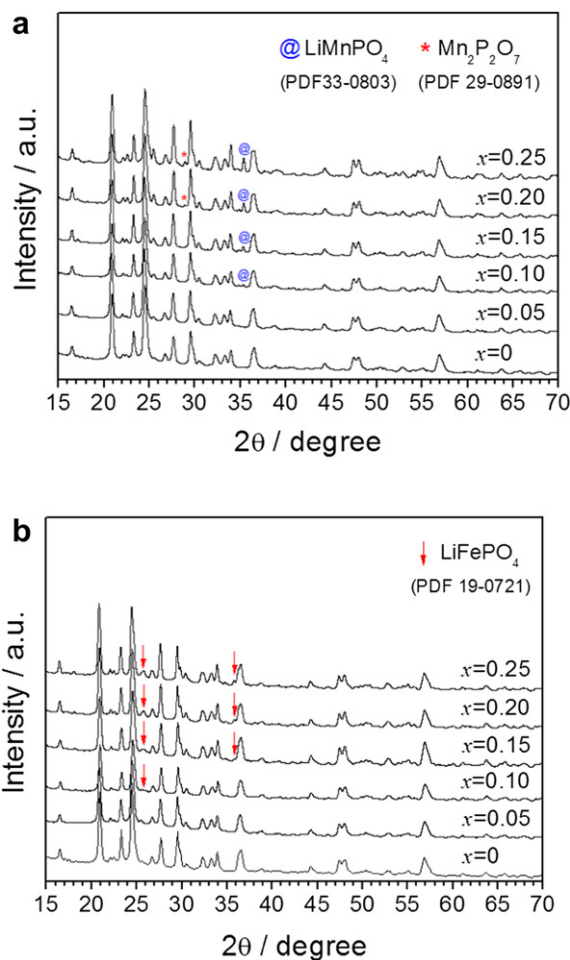


Fig. 1. XRD patterns of $\text{Li}_3\text{V}_{2-2x}\text{Ti}_x\text{Mn}_x(\text{PO}_4)_3$ (a) and $\text{Li}_3\text{V}_{2-2x}\text{Ti}_x\text{Fe}_x(\text{PO}_4)_3$ (b) ($x = 0, 0.05, 0.1, 0.15, 0.20, 0.25$).

to 0.1. The diffraction peak at 35° (denoted by at sign) in the XRD patterns of the Ti and Mn codoped samples (Fig. 1(a)) can be attributed to LiMnPO_4 (PDF 33-0803), while the diffraction peaks at 25.6° and 35.7° (denoted by arrow) in the XRD patterns of the Ti and Fe codoped samples (Fig. 1(b)) can be attributed to LiFePO_4 (PDF 19-0721). An additional diffraction peak at 28.9° (denoted by asterisk) begins to appear in Fig. 1(a) when x is further increased to 0.2, and it can be attributed to $\text{Mn}_2\text{P}_2\text{O}_7$ (PDF 29-0891). Furthermore, the peak intensities of impurities in the XRD patterns increase with x . Therefore, single phase $\text{Li}_3\text{V}_{2-2x}\text{Ti}_x\text{Mn}_x(\text{PO}_4)_3$ and $\text{Li}_3\text{V}_{2-2x}\text{Ti}_x\text{Fe}_x(\text{PO}_4)_3$ can be prepared only if x is not higher than 0.05.

No diffraction peak of carbon is observed in the XRD pattern of each sample, which indicates the amorphous nature of the residual carbon. The carbon contents of $\text{Li}_3\text{V}_{2-2x}\text{Ti}_x\text{Mn}_x(\text{PO}_4)_3$ ($x = 0, 0.05, 0.1, 0.15, 0.20$ and 0.25) are 4.11%, 4.19%, 4.28%, 4.36%, 4.45% and 4.51%, respectively, and those of $\text{Li}_3\text{V}_{2-2x}\text{Ti}_x\text{Fe}_x(\text{PO}_4)_3$ ($x = 0, 0.05, 0.1, 0.15, 0.20$ and 0.25) are 4.11%, 4.16%, 4.23%, 4.29%, 4.35% and 4.40%, respectively.

The lattice parameters of the single phase samples, i.e. $\text{Li}_3\text{V}_{1.9}\text{Ti}_{0.05}\text{Mn}_{0.05}(\text{PO}_4)_3$, $\text{Li}_3\text{V}_{1.9}\text{Ti}_{0.05}\text{Fe}_{0.05}(\text{PO}_4)_3$ and $\text{Li}_3\text{V}_2(\text{PO}_4)_3$, are calculated, and the results are listed in Table 1. The lattice parameters (a , b , c and V) of the Ti–Mn or Ti–Fe codoped sample are larger than those of the undoped sample. The expansion of crystal lattice can make room for lithium ion diffusion, which is of benefit to the electrochemical performance. The change of the lattice

Table 1

Lattice parameters of $\text{Li}_3\text{V}_2(\text{PO}_4)_3$, $\text{Li}_3\text{V}_{1.9}\text{Ti}_{0.05}\text{Mn}_{0.05}(\text{PO}_4)_3$ and $\text{Li}_3\text{V}_{1.9}\text{Ti}_{0.05}\text{Fe}_{0.05}(\text{PO}_4)_3$.

Sample	<i>a</i>	<i>b</i>	<i>c</i>	β	<i>V</i>
$\text{Li}_3\text{V}_2(\text{PO}_4)_3$	8.5540(3)	8.5720(4)	12.0129(6)	90.12	880.8
$\text{Li}_3\text{V}_{1.9}\text{Ti}_{0.05}\text{Mn}_{0.05}(\text{PO}_4)_3$	8.5805(7)	8.6327(1)	12.0225(6)	90.51	890.5
$\text{Li}_3\text{V}_{1.9}\text{Ti}_{0.05}\text{Fe}_{0.05}(\text{PO}_4)_3$	8.5747(6)	8.5925(1)	12.0297(6)	90.35	886.3

parameters is induced by the difference between the radii of Ti and Mn or Ti and Fe and the radius of V. However, the radii of the dopants are affected by their oxidation states. Therefore, it is necessary to measure the oxidation states of the dopants (Ti, Mn and Fe).

3.2. XPS characterization

The oxidation states of V, Ti, Mn and Fe were determined by XPS measurements. Fig. 2 shows the XPS spectra of V2p, Ti2p and Mn2p in $\text{Li}_3\text{V}_{1.9}\text{Ti}_{0.05}\text{Mn}_{0.05}(\text{PO}_4)_3$ (left column) and V2p, Ti2p and Fe2p in $\text{Li}_3\text{V}_{1.9}\text{Ti}_{0.05}\text{Fe}_{0.05}(\text{PO}_4)_3$ (right column). The XPS spectra of V2p and Ti2p in $\text{Li}_3\text{V}_{1.9}\text{Ti}_{0.05}\text{Mn}_{0.05}(\text{PO}_4)_3$ are very similar to those in $\text{Li}_3\text{V}_{1.9}\text{Ti}_{0.05}\text{Fe}_{0.05}(\text{PO}_4)_3$. Both the XPS spectra of V2p have two

peaks, which is due to the spin-orbit coupling. The major peak at 517.1 eV and the satellite peak at 523.4 eV can be assigned to $\text{V}2\text{p}_{3/2}$ and $\text{V}2\text{p}_{1/2}$, respectively [19]. The binding energies of both peaks indicate that the oxidation states of V in both Ti–Mn and Ti–Fe codoped samples are +3. Both the XPS spectra of Ti2p also have two peaks. The major peak at 459.2 eV and the satellite peak at 465.2 eV can be assigned to $\text{Ti}2\text{p}_{3/2}$ and $\text{Ti}2\text{p}_{1/2}$, respectively. The binding energies of both peaks are the same as those of TiO_2 [20], thus the oxidation states of Ti in both Ti–Mn and Ti–Fe codoped samples are +4. The XPS spectrum of Mn2p can be split into two spectra, i.e. $\text{Mn}2\text{p}_{1/2}$ and $\text{Mn}2\text{p}_{3/2}$. The $\text{Mn}2\text{p}_{1/2}$ spectrum has a single peak at 654.2 eV. The $\text{Mn}2\text{p}_{3/2}$ spectrum has a major peak at 641.5 eV and a satellite peak at 646.6 eV. The binding energies of the peaks are similar to those of MnO [21,22], which indicates that the oxidation state of Mn in $\text{Li}_3\text{V}_{1.9}\text{Ti}_{0.05}\text{Mn}_{0.05}(\text{PO}_4)_3$ is +2. The Fe2p spectrum, which has a single peak at 710.5 eV, can be assigned to $\text{Fe}2\text{p}_{3/2}$. The binding energy of the peak is the same as that of LiFePO_4 [19], which verifies that the oxidation state of Fe in $\text{Li}_3\text{V}_{1.9}\text{Ti}_{0.05}\text{Fe}_{0.05}(\text{PO}_4)_3$ is +2. Therefore, the oxidation of Ti, Mn, Fe and V are respectively +4, +2, +2 and +3. The radius of Ti^{4+} (0.61 Å) is slightly smaller than that of V^{3+} (0.64 Å), while the radius of Mn^{2+} (0.83 Å) or Fe^{2+} (0.78 Å) is much larger than that of V^{3+} , thus the expansion of crystal lattice in $\text{Li}_3\text{V}_{1.9}\text{Ti}_{0.05}\text{Mn}_{0.05}(\text{PO}_4)_3$ or

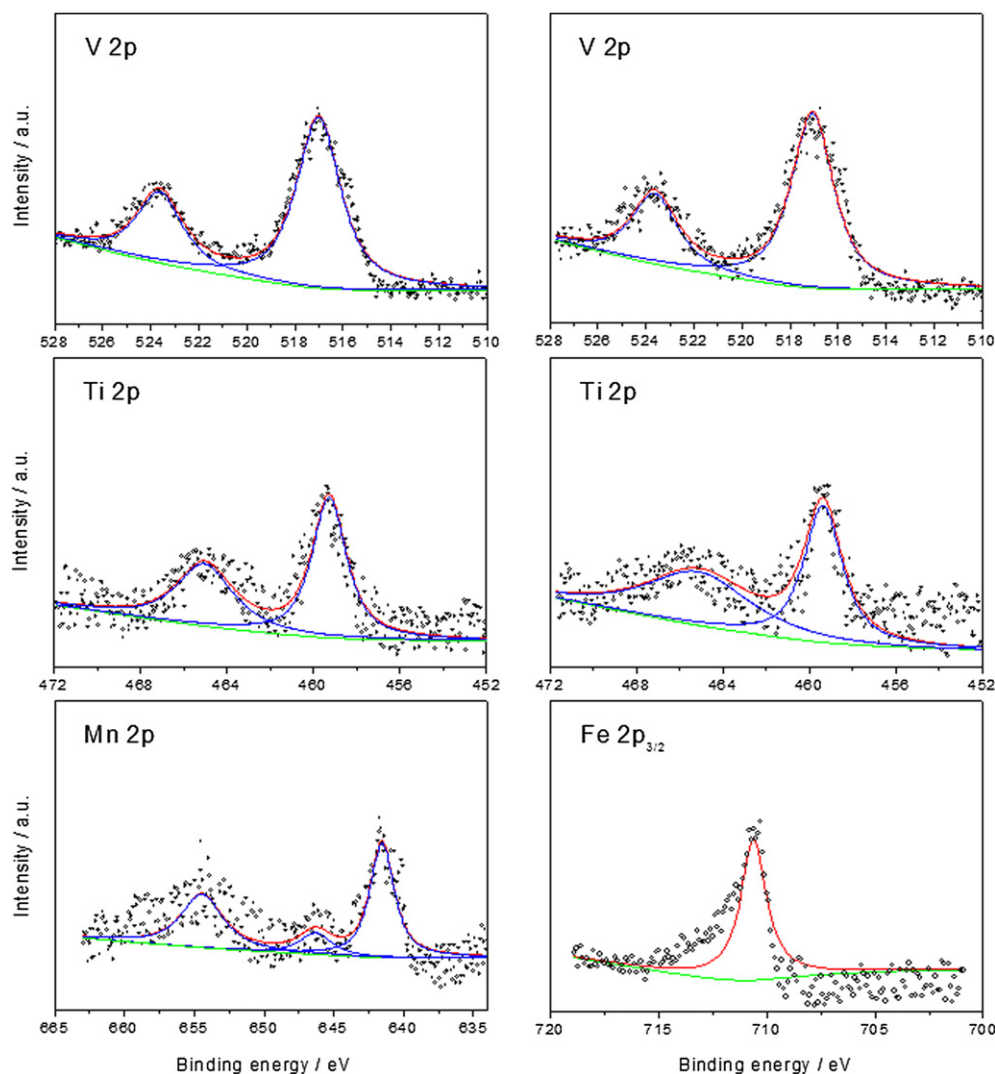


Fig. 2. XPS spectra of V2p, Ti2p and Mn2p in the $\text{Li}_3\text{V}_{1.9}\text{Ti}_{0.05}\text{Mn}_{0.05}(\text{PO}_4)_3$ (left column) and V2p, Ti2p and Fe2p in $\text{Li}_3\text{V}_{1.9}\text{Ti}_{0.05}\text{Fe}_{0.05}(\text{PO}_4)_3$ (right column).

$\text{Li}_3\text{V}_{1.9}\text{Ti}_{0.05}\text{Fe}_{0.05}(\text{PO}_4)_3$ can be attributed to Mn^{2+} or Fe^{2+} rather than Ti^{4+} [23].

3.3. First charge-discharge cycle

3.3.1. Ti and Mn codoped samples

All the Ti–Mn and Ti–Fe codoped samples were cycled at a current density of 0.2 C in the voltage range of 3.0–4.8 V, where 1 C rate corresponds to the current density of 180 mA g^{-1} Fig. 3(a) shows the first charge/discharge curves of the Ti and Mn codoped samples. Four plateaus are observed respectively at 3.63, 3.69, 4.10 and 4.60 V for $\text{Li}_3\text{V}_2(\text{PO}_4)_3$ ($x = 0$). Each plateau corresponds to a phase transition processes between two adjacent single phases of $\text{Li}_y\text{V}_2(\text{PO}_4)_3$ ($y = 3.0, 2.5, 2.0, 1.0$ and 0). The extractions of the first two and the third lithium ions are associated with the $\text{V}^{3+}/\text{V}^{4+}$ and the $\text{V}^{4+}/\text{V}^{5+}$ redox couples, respectively.

Ti and Mn codoping induce some changes in the first charge curves. In order to clarify the changes, the capacity ratio of the third plateau to the first two plateaus is calculated, and the results are shown in Fig. 4. The first two plateaus correspond to the extraction of the first lithium ion, while the third plateau corresponds to the extraction of the second lithium ion. Therefore, the theoretical value of the capacity ratio is 1 for $\text{Li}_3\text{V}_2(\text{PO}_4)_3$. The experimental value in Fig. 4 is very close to the theoretical one. However, Ti and Mn codoping has profound effect on the capacity ratio. The capacity ratio first increase with x , reach a maximum value at $x = 0.1$, and then turn to decrease with x . Whether the capacity ratio increases or decreases with x , it is always higher than 1. These phenomena can be associated with the incorporation of Mn^{2+} . Whether Mn^{2+} enters into the bulk structure or forms as LiMnPO_4 , the oxidation potential of $\text{Mn}^{2+}/\text{Mn}^{3+}$ is close the potential of the third plateau in the charge curve [7]. This results in the increase of the capacity ratio with x . However, the utilization of LiMnPO_4 declines with an

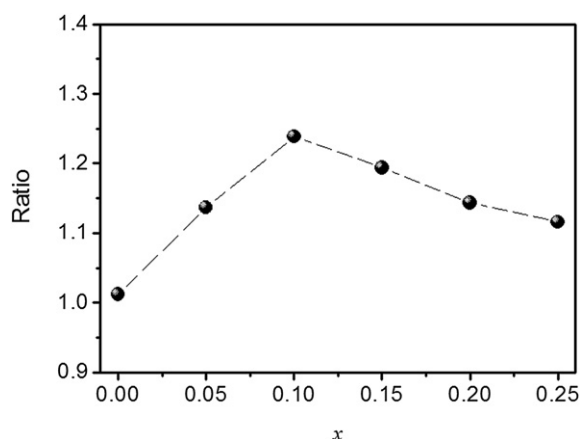


Fig. 4. The capacity ratio of the third plateau to the first two plateaus in the first charge curve of $\text{Li}_3\text{V}_{2-2x}\text{Ti}_x\text{Mn}_x(\text{PO}_4)_3$ ($x = 0, 0.05, 0.1, 0.15, 0.20, 0.25$).

increase in crystallinity, and $\text{Mn}_2\text{P}_2\text{O}_7$, which also forms as an impurity, is electrochemically inert. The increases in the crystallinity of LiMnPO_4 and the amount of $\text{Mn}_2\text{P}_2\text{O}_7$ lead to the decrease of the capacity ratio with x , but neither factor can make the capacity ratio decrease less than 1.

Fig. 5(a) shows the differential capacity vs. voltage (dQ/dE vs. E) curves of $\text{Li}_3\text{V}_{2-2x}\text{Ti}_x\text{Mn}_x(\text{PO}_4)_3$. The dQ/dE vs. E curves provide information similar to that of the cyclic voltammograms. The peaks in the dQ/dE vs. E curves correspond to the plateaus in the charge/discharge curves. Four oxidation peaks and three reduction peaks are clearly observed in each dQ/dE vs. E curve. The potential difference between the oxidation peak and reduction peak increases with x , which indicates that the electrochemical polarization increase with x . Compared with the last oxidation peak of

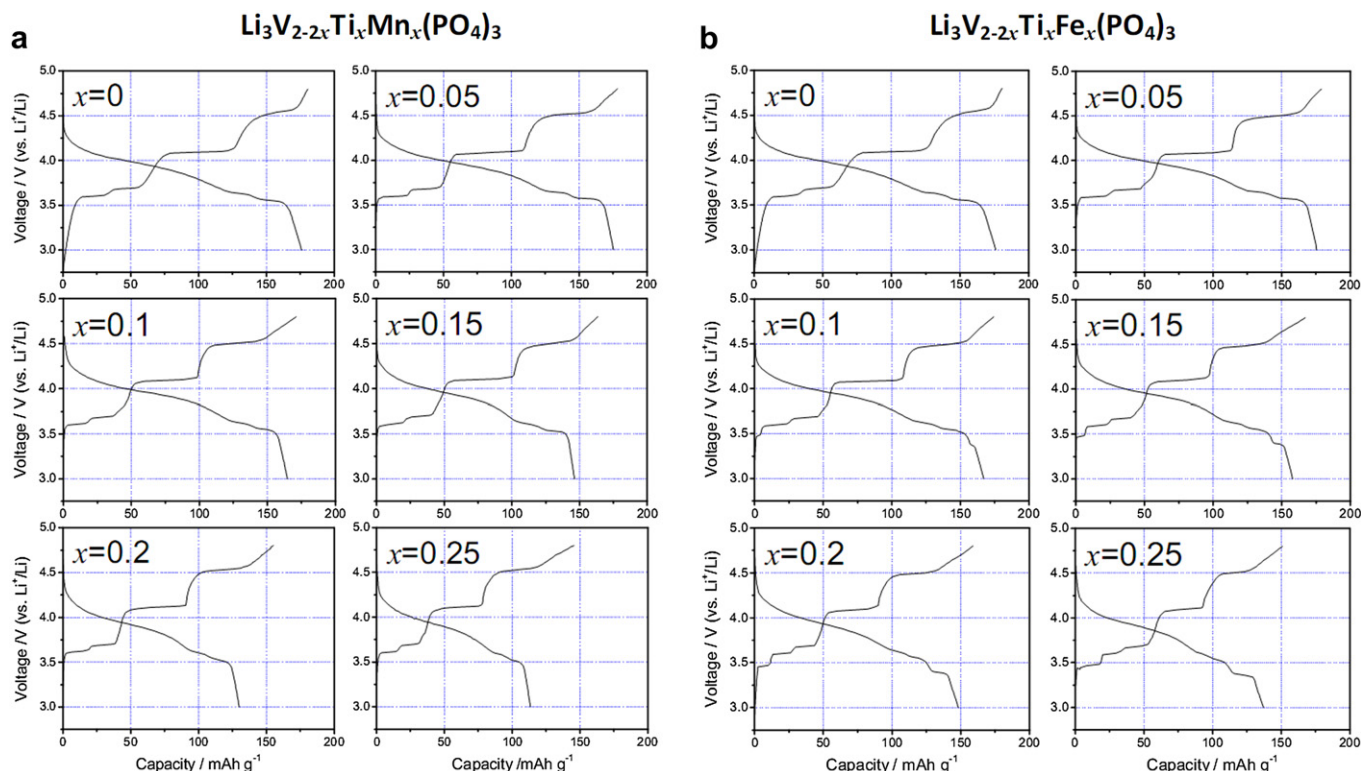


Fig. 3. The first charge/discharge curves of $\text{Li}_3\text{V}_{2-2x}\text{Ti}_x\text{Mn}_x(\text{PO}_4)_3$ (a) And $\text{Li}_3\text{V}_{2-2x}\text{Ti}_x\text{Fe}_x(\text{PO}_4)_3$ (b) ($x = 0, 0.05, 0.1, 0.15, 0.20$ and 0.25).

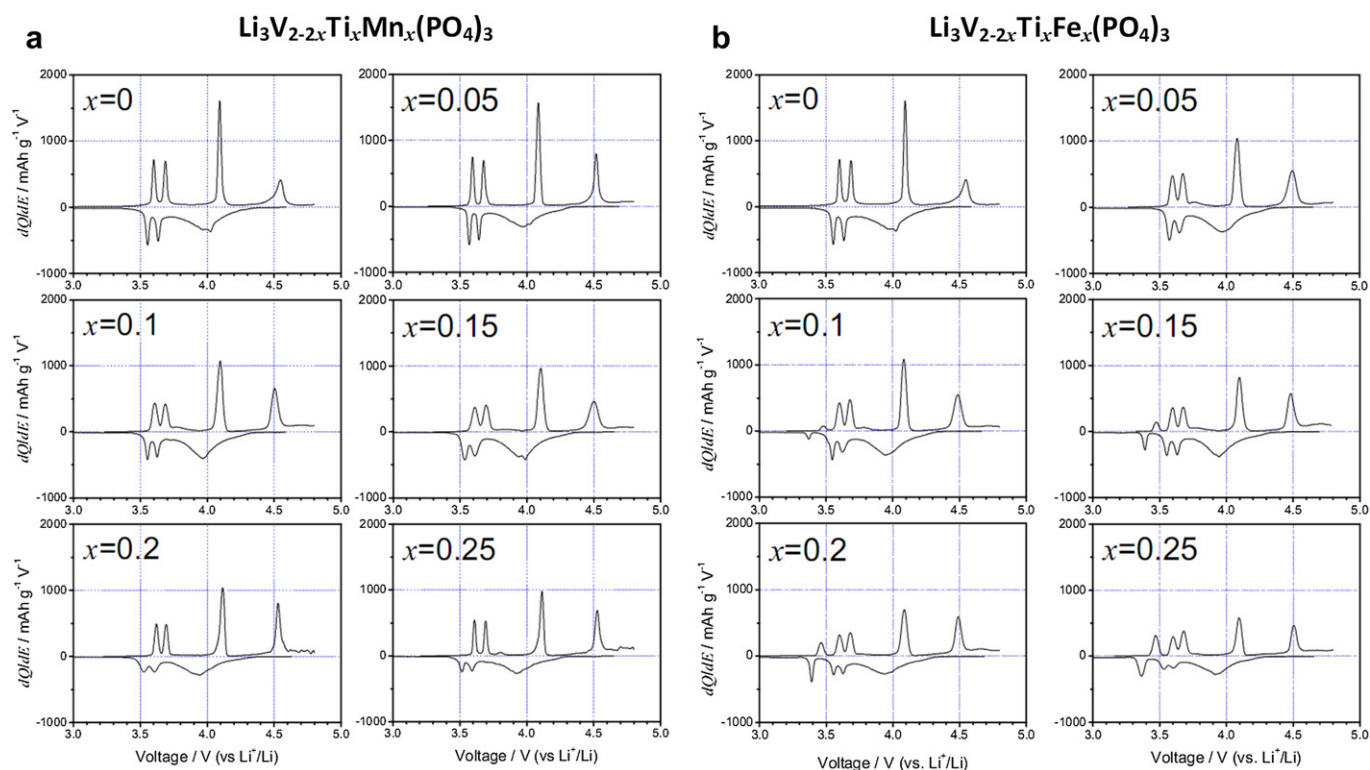


Fig. 5. The differential capacity vs. voltage curves of $\text{Li}_3\text{V}_{2-2x}\text{Ti}_x\text{Mn}_x(\text{PO}_4)_3$ (a) And $\text{Li}_3\text{V}_{2-2x}\text{Ti}_x\text{Fe}_x(\text{PO}_4)_3$ (b) ($x = 0, 0.05, 0.1, 0.15, 0.20$ and 0.25).

the undoped sample, the last oxidation peak of the Ti and Mn codoped samples shift to lower voltage. This indicates that Ti and Mn codoping can lower the oxidation potential of $\text{V}^{4+}/\text{V}^{5+}$.

Fig. 6 shows the first charge/discharge capacity and the first cycle columbic efficiency of $\text{Li}_3\text{V}_{2-2x}\text{Ti}_x\text{Mn}_x(\text{PO}_4)_3$. The charge/discharge capacity monotonously decreases with x , because Ti^{4+} is electrochemically inert. Moreover, the presence of impurities can further decrease the charge/discharge capacity. The columbic efficiency first increase with x , reach a maximum value at $x = 0.05$, and then turn to decrease with x . The stabilization effect of Ti^{4+} results in the initial increase of columbic efficiency, while the detrimental effect of the impurities leads to the subsequent decrease.

3.3.2. Ti and Fe codoped samples

The first charge/discharge curves of $\text{Li}_3\text{V}_{2-2x}\text{Ti}_x\text{Fe}_x(\text{PO}_4)_3$ are shown in Fig. 3(b). The first charge/discharge curve of

$\text{Li}_3\text{V}_{1.9}\text{Ti}_{0.05}\text{Fe}_{0.05}(\text{PO}_4)_3$ in Fig. 3(b) is similar to that of $\text{Li}_3\text{V}_2(\text{PO}_4)_3$, and no extra plateau is observed. An additional pair of plateaus, a charge plateau at 3.48 V and a discharge plateau at 3.38 V, begins to appear in the charge-discharge curves when x is further increased to 0.1. The capacity involved in this pair of plateaus increase with x .

Two ratios are calculated in order to clarify the change of charge curve with x , and the results are shown in Fig. 7. There are five plateaus in the charge curve if x is no lower than 0.1. If all the five plateaus are taken into account, a ratio (R_I) is the capacity ratio of the first plateau to the second and third plateaus, and the other ratio (R_{II}) is the capacity of the fourth plateau to the second and third plateaus. Therefore, R_I is equal to 0 if x is not higher than 0.05. Once the first plateau appears, R_I monotonously increases with x . The result is associated with the impurities in Ti and Fe codoped

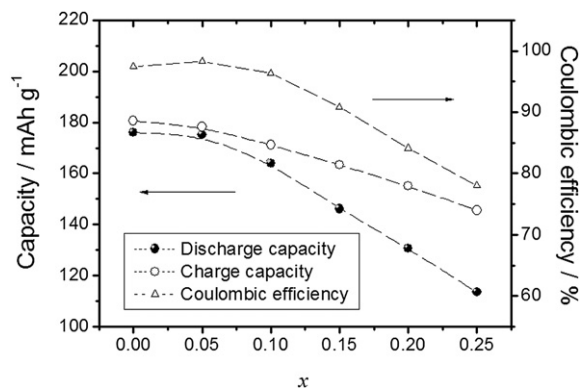


Fig. 6. The first charge/discharge capacity and the first cycle columbic efficiency of $\text{Li}_3\text{V}_{2-2x}\text{Ti}_x\text{Mn}_x(\text{PO}_4)_3$ ($x = 0, 0.05, 0.1, 0.15, 0.20, 0.25$).

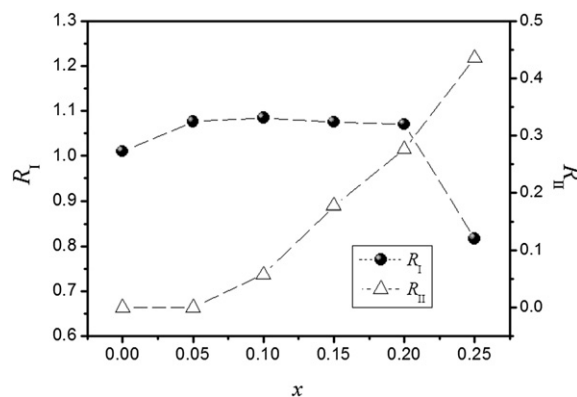


Fig. 7. The capacity ratio of the first plateau to the second and third plateaus (R_I) and the capacity ratio of the fourth plateau to the second and third plateaus (R_{II}) of $\text{Li}_3\text{V}_{2-2x}\text{Ti}_x\text{Fe}_x(\text{PO}_4)_3$ ($x = 0, 0.05, 0.1, 0.15, 0.20, 0.25$).

samples. The variation of R_i can wholly be attributed to the appearance and increase of the impurity phase, i.e. LiFePO_4 . The charge plateau of LiFePO_4 has a potential of ca 3.45 V that is nearly the same as the potential of the first charge plateau [19,24]. R_{ii} first increase slightly with x , and then keeps nearly unchanged when x increases from 0.05 to 0.2, and finally decrease dramatically with x . The slightly increase can be attributed to the incorporation of Fe^{2+} into the bulk structure. The amount of incorporated Fe^{2+} keeps nearly constant when x increases from 0.05 to 0.2, because the residual Fe^{2+} turns into the form of LiFePO_4 . The formation of LiFePO_4 induces structural deficiency in the bulk structure. When x reaches 0.25, the structural deficiency is so severe that the structural instability manifests itself, especially at a higher charge potential. This leads to the shrinkage of the plateaus. The higher the potential, the severer the shrinkage. Thus R_{ii} dramatically decrease.

The differential capacity vs. voltage curves of $\text{Li}_3\text{V}_{2-2x}\text{Ti}_x\text{Fe}_x(\text{PO}_4)_3$ are shown in Fig. 5(b). The redox peaks become boarder after Ti and Fe codoping, which indicate that Ti and Fe codoping induces structural disorder. An additional pair of redox peaks at about ca 3.45 V begins to appear at $x = 0.10$, and they become sharper when x further increases because the amount of impurity, i.e. LiFePO_4 , increases with x . The last oxidation peak shift to lower potentials after Ti and Fe codoping, which indicates that Ti and Fe codoping lowers the oxidation potential of $\text{V}^{4+}/\text{V}^{5+}$.

Fig. 8 shows the first charge/discharge capacity and the first cycle columbic efficiency of $\text{Li}_3\text{V}_{2-2x}\text{Ti}_x\text{Fe}_x(\text{PO}_4)_3$. Both charge capacity and discharge capacity decline with an increase in x because Ti^{4+} is electrochemically inert. Although the impurity, i.e. LiFePO_4 , is electrochemical active, its capacity is not as high as that of $\text{Li}_3\text{V}_2(\text{PO}_4)_3$. The columbic efficiency also decreases with x , which indicates that the structural stability decrease with x .

3.4. Rate capability and cycle performance

According to the structural characterization, only $\text{Li}_3\text{V}_{1.9}\text{Ti}_{0.05}\text{Mn}_{0.05}(\text{PO}_4)_3$ and $\text{Li}_3\text{V}_{1.9}\text{Ti}_{0.05}\text{Fe}_{0.05}(\text{PO}_4)_3$ are single phase. Their first cycle performance are slightly poorer than that of $\text{Li}_3\text{V}_2(\text{PO}_4)_3$. Therefore, only these three samples are further characterized.

Fig. 9 shows the Rate capability of $\text{Li}_3\text{V}_2(\text{PO}_4)_3$, $\text{Li}_3\text{V}_{1.9}\text{Ti}_{0.05}\text{Mn}_{0.05}(\text{PO}_4)_3$ and $\text{Li}_3\text{V}_{1.9}\text{Ti}_{0.05}\text{Fe}_{0.05}(\text{PO}_4)_3$. All the cells were charged at 0.2 C and then discharged at various current densities, i.e. 0.1 C, 0.2 C, 0.3 C, 0.5 C, 1 C, 5 C, 10 C and 20 C. The discharge capacity of each sample declines with an increase in current density. The discharge capacity of $\text{Li}_3\text{V}_2(\text{PO}_4)_3$ is the highest when the current density is not higher than 0.3 C. However, the discharge capacity of $\text{Li}_3\text{V}_{1.9}\text{Ti}_{0.05}\text{Fe}_{0.05}(\text{PO}_4)_3$ becomes the highest when the

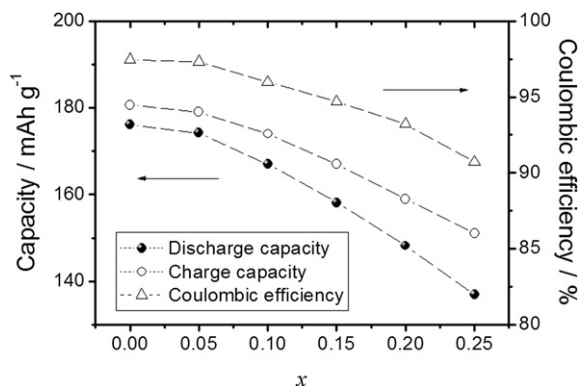


Fig. 8. The first charge/discharge capacity and the first cycle columbic efficiency of $\text{Li}_3\text{V}_{2-2x}\text{Ti}_x\text{Fe}_x(\text{PO}_4)_3$ ($x = 0, 0.05, 0.1, 0.15, 0.20, 0.25$).

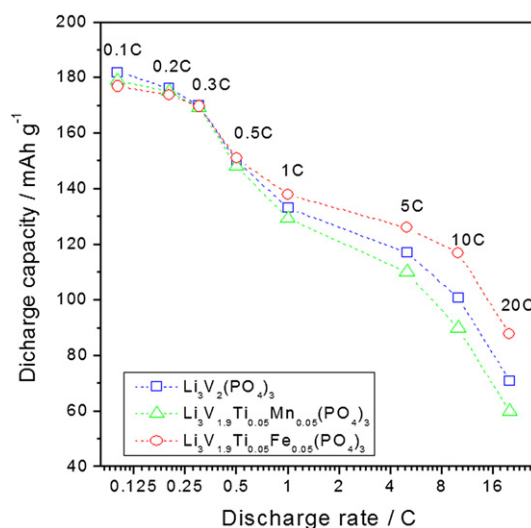


Fig. 9. Rate capability of $\text{Li}_3\text{V}_{1.9}\text{Ti}_{0.05}\text{Mn}_{0.05}(\text{PO}_4)_3$, $\text{Li}_3\text{V}_{1.9}\text{Ti}_{0.05}\text{Fe}_{0.05}(\text{PO}_4)_3$ and $\text{Li}_3\text{V}_2(\text{PO}_4)_3$.

current density is 0.5 C or higher. These results indicate that a small amount of Ti and Fe codoping can improve the discharge capacity only if the current density is high enough.

The cycle performance of $\text{Li}_3\text{V}_{1.9}\text{Ti}_{0.05}\text{Mn}_{0.05}(\text{PO}_4)_3$, $\text{Li}_3\text{V}_{1.9}\text{Ti}_{0.05}\text{Fe}_{0.05}(\text{PO}_4)_3$ and $\text{Li}_3\text{V}_2(\text{PO}_4)_3$ at the current densities of 5 C and 10 C are shown in Fig. 10(a) and (b), respectively. The capacity decreases

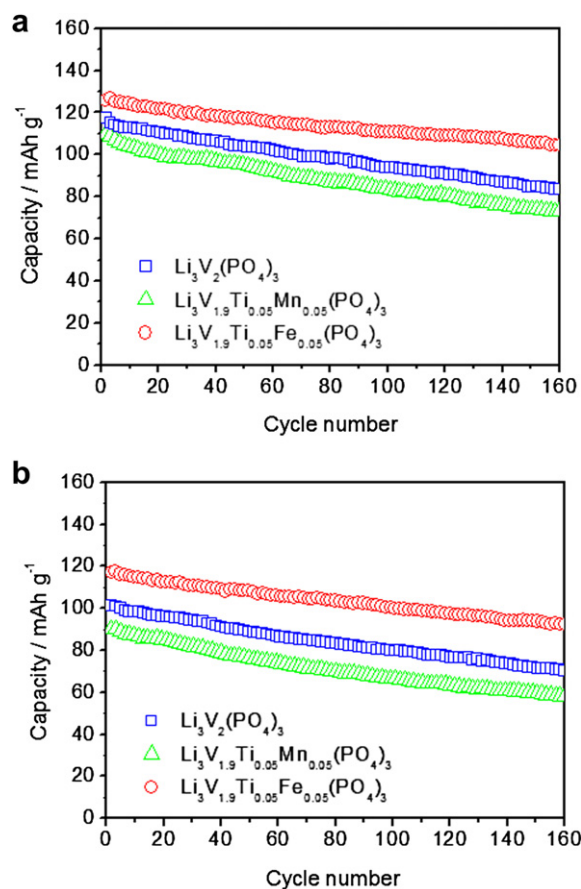


Fig. 10. Cycle performance of $\text{Li}_3\text{V}_{1.9}\text{Ti}_{0.05}\text{Mn}_{0.05}(\text{PO}_4)_3$, $\text{Li}_3\text{V}_{1.9}\text{Ti}_{0.05}\text{Fe}_{0.05}(\text{PO}_4)_3$ and $\text{Li}_3\text{V}_2(\text{PO}_4)_3$ at the current densities of 5 C (a) and 10 C (b).

with increased cycle number for all the samples. Several possible reasons such as loss of crystallinity, decomposition of electrolyte and dissolution of vanadium were proposed for this capacity fading [5,25–27]. There is a little loss of crystallinity in the $V_2(PO_4)_3$ phase when all the lithium ions are extracted [25]. Progressive dissolution of vanadium in the electrolyte and decomposition of electrolyte are favored by the high oxidative potential, i.e. 4.8 V [5,26,27]. Whether the current density is 5 C or 10 C, the capacity retention of $Li_3V_{1.9}Ti_{0.05}Fe_{0.05}(PO_4)_3$ is the highest, while that of $Li_3V_{1.9}Ti_{0.05}Mn_{0.05}(PO_4)_3$ is the lowest. The best cycle stability of $Li_3V_{1.9}Ti_{0.05}Fe_{0.05}(PO_4)_3$ can be attributed to the structural stabilization effect induced by Ti and Fe codoping. The ionic radii of V^{3+} , V^{4+} and V^{5+} are 0.64 Å, 0.58 Å, and 0.355 Å, respectively [23]. The oxidation state of V increases/decreases to the accompaniment of lithium deintercalation/intercalation during the charge/discharge process, and the crystal lattice shrinks/expands at the same time. Ti^{4+} is electrochemically inert, and thus its radius does not change during charge/discharge cycling. The ionic radii of Fe^{2+} and Fe^{3+} are 0.78 Å and 0.645 Å, respectively [23]. The shuttle between Fe^{2+} and Fe^{3+} induces less structural change compared with the shuttle between V^{3+} and V^{5+} [28]. Therefore, Ti and Fe codoping can lessen the distortion of crystal lattice during charge and can thus improve the cycle performance. The worst cycle stability of $Li_3V_{1.9}Ti_{0.05}Mn_{0.05}(PO_4)_3$ is due to the instable Mn^{3+} , which is the oxidation product Mn^{2+} . It is well known that Mn^{3+} is structurally unstable and can lead to dramatic distortion of crystal lattice [29,30]. The beneficial effect of Ti^{4+} cannot counteract the detrimental effect of Mn^{2+} . Therefore, Ti and Mn codoping have a detrimental effect on cycle performance.

Although the incorporation of Ti^{4+} cannot expand the crystal lattice, it has the advantage of keeping charge neutrality and stabilizing crystal lattice in $Li_3V_{1.9}Ti_{0.05}Fe_{0.05}(PO_4)_3$. Charge imbalance will be induced if only Fe^{2+} or Mn^{2+} is doped at V^{3+} site. Doping equimolar Ti^{4+} and Fe^{2+} (or Mn^{2+}) at V^{3+} site can make charge balance. In addition, Ti^{4+} is electrochemically inert in the potential range of 3–4.8 V, thus it can stabilize the crystal lattice during cycling and help to sustain the crystallinity.

$Li_3V_{1.95}Fe_{0.05}(PO_4)_3$ is prepared to examine what will happen if no Ti^{4+} but Fe^{2+} is doped. The XRD pattern of $Li_3V_{1.95}Fe_{0.05}(PO_4)_3$ are shown in Fig. 11, it has no extra diffraction peaks in comparison to the XRD patterns of $Li_3V_2(PO_4)_3$ and $Li_3V_{1.9}Ti_{0.05}Fe_{0.05}(PO_4)_3$, which indicates that Fe^{2+} are successfully incorporated into the bulk structure of $Li_3V_{1.95}Fe_{0.05}(PO_4)_3$. Fig. 12 shows the cycling performance of $Li_3V_{1.95}Fe_{0.05}(PO_4)_3$ and $Li_3V_{1.9}Ti_{0.05}Fe_{0.05}(PO_4)_3$ at the current densities of 0.5 C and 5 C. Although $Li_3V_{1.95}Fe_{0.05}(PO_4)_3$

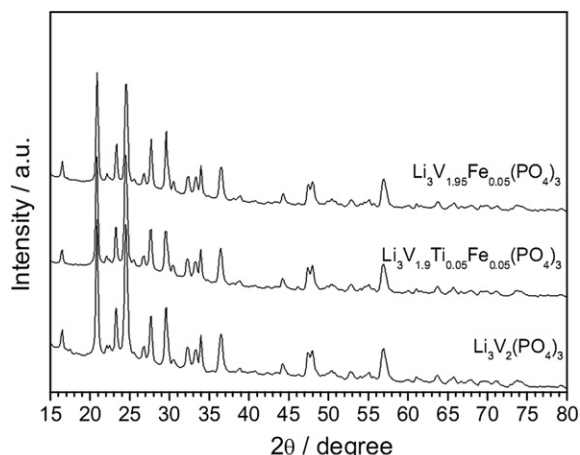


Fig. 11. XRD patterns of $Li_3V_2(PO_4)_3$, $Li_3V_{1.9}Ti_{0.05}Fe_{0.05}(PO_4)_3$ and $Li_3V_{1.95}Fe_{0.05}(PO_4)_3$.

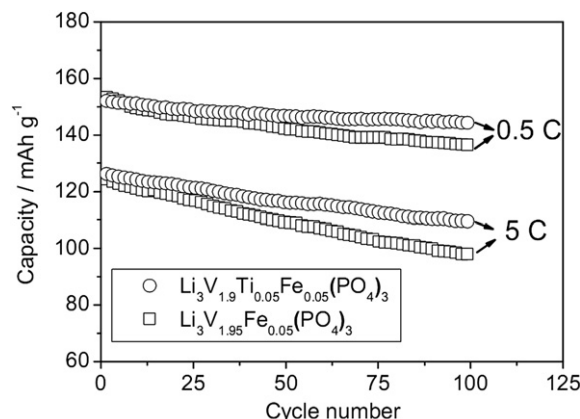


Fig. 12. Cycling performance of $Li_3V_{1.95}Fe_{0.05}(PO_4)_3$ and $Li_3V_{1.9}Ti_{0.05}Fe_{0.05}(PO_4)_3$ at the current densities of 0.5 C and 5 C.

has a slightly higher capacity at 0.5 C, it suffers from a severer capacity fading at both 0.5 C and 5 C. Moreover, the cycling performance of $Li_3V_{1.95}Fe_{0.05}(PO_4)_3$ is more inferior to that of $Li_3V_{1.9}Ti_{0.05}Fe_{0.05}(PO_4)_3$ when the current density is higher. Therefore, the improved cycling performance of $Li_3V_{1.9}Ti_{0.05}Fe_{0.05}(PO_4)_3$ can be attributed to the stabilization effect of Ti^{4+} .

3.5. Morphological observation

Fig. 13 shows the SEM images of $Li_3V_2(PO_4)_3$, $Li_3V_{1.9}Ti_{0.05}Mn_{0.05}(PO_4)_3$ and $Li_3V_{1.9}Ti_{0.05}Fe_{0.05}(PO_4)_3$. All the samples are composed of irregular particles, and their particle size distributions are broad. The particles are loosely packed together, which makes them have a porous structure. The particle sizes of $Li_3V_{1.9}Ti_{0.05}Mn_{0.05}(PO_4)_3$ and $Li_3V_{1.9}Ti_{0.05}Fe_{0.05}(PO_4)_3$ are smaller than that of $Li_3V_2(PO_4)_3$. A smaller particle size can shorten the path for solid-state diffusion and enlarge the area for charge transfer reaction, thus it can enhance the discharge capacity at high current density. This beneficial effect of smaller particle size partly contributes to the higher discharge capacity of $Li_3V_{1.9}Ti_{0.05}Fe_{0.05}(PO_4)_3$ at the current density of 0.5–20 C, while it cannot counteract the detrimental effect of Mn^{2+} in $Li_3V_{1.9}Ti_{0.05}Mn_{0.05}(PO_4)_3$.

In order to clarify whether the smaller particle size or the larger lattice volume of $Li_3V_{1.9}Ti_{0.05}Fe_{0.05}(PO_4)_3$ plays a vital role in

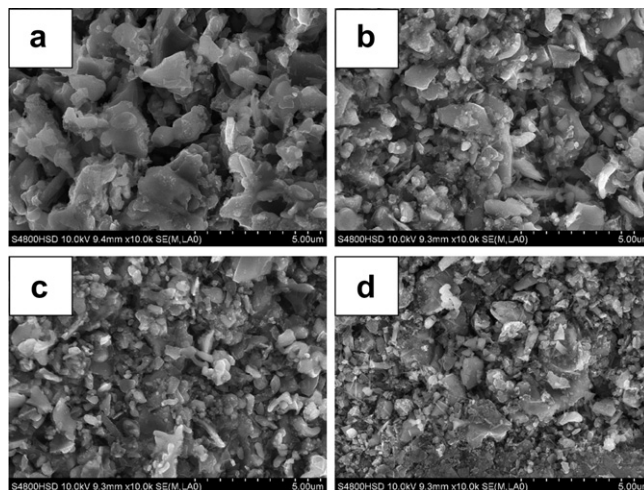


Fig. 13. SEM images of $Li_3V_2(PO_4)_3$ (a), $Li_3V_{1.9}Ti_{0.05}Mn_{0.05}(PO_4)_3$ (b), $Li_3V_{1.9}Ti_{0.05}Fe_{0.05}(PO_4)_3$ (c) And ball-milled $Li_3V_2(PO_4)_3$ (d).

improving the rate capability, the $\text{Li}_3\text{V}_2(\text{PO}_4)_3$ sample should be milled to a particle size similar to that of $\text{Li}_3\text{V}_{1.9}\text{Ti}_{0.05}\text{Fe}_{0.05}(\text{PO}_4)_3$. The SEM image of the ball-milled $\text{Li}_3\text{V}_2(\text{PO}_4)_3$ is shown in Fig. 13(d). The particle size of the ball-milled $\text{Li}_3\text{V}_2(\text{PO}_4)_3$ is smaller than that of the pristine $\text{Li}_3\text{V}_2(\text{PO}_4)_3$ and similar to that of $\text{Li}_3\text{V}_{1.9}\text{Ti}_{0.05}\text{Fe}_{0.05}(\text{PO}_4)_3$.

The rate capability of the ball-milled $\text{Li}_3\text{V}_2(\text{PO}_4)_3$ is shown in Fig. 14, and that of $\text{Li}_3\text{V}_{1.9}\text{Ti}_{0.05}\text{Fe}_{0.05}(\text{PO}_4)_3$ is shown as a reference. Each cell was charged at 0.2 C and then discharged at various current densities. Although the discharge capacity of the ball-milled $\text{Li}_3\text{V}_2(\text{PO}_4)_3$ is higher than that of $\text{Li}_3\text{V}_{1.9}\text{Ti}_{0.05}\text{Fe}_{0.05}(\text{PO}_4)_3$ when the current density is not higher than 0.3 C, it is reversed when the current density is not lower than 0.5 C. The improved high-rate capability of $\text{Li}_3\text{V}_{1.9}\text{Ti}_{0.05}\text{Fe}_{0.05}(\text{PO}_4)_3$ can be attributed to its larger lattice volume because the particle sizes of both samples are similar. However, the discharge capacity of the ball-milled $\text{Li}_3\text{V}_2(\text{PO}_4)_3$ is higher than that of the pristine $\text{Li}_3\text{V}_2(\text{PO}_4)_3$ (Fig. 9) when the current density is not lower than 1 C. Therefore, both smaller particle size and larger lattice volume play a role in the better high-rate capability of $\text{Li}_3\text{V}_{1.9}\text{Ti}_{0.05}\text{Fe}_{0.05}(\text{PO}_4)_3$. What's more, the larger lattice volume plays a more important role.

3.6. EIS measurements

Fig. 15 shows the Nyquist plots of $\text{Li}_3\text{V}_2(\text{PO}_4)_3$, $\text{Li}_3\text{V}_{1.9}\text{Ti}_{0.05}\text{Mn}_{0.05}(\text{PO}_4)_3$ and $\text{Li}_3\text{V}_{1.9}\text{Ti}_{0.05}\text{Fe}_{0.05}(\text{PO}_4)_3$. All the electrodes were prepared in the same way and cycled twenty times before EIS measurement. Each Nyquist plot consists of a depressed semicircle and a sloping line. The depressed semicircle and the sloping line can be respectively attributed to charge transfer reaction and solid-state diffusion of lithium ion. The depressed semicircle of $\text{Li}_3\text{V}_{1.9}\text{Ti}_{0.05}\text{Fe}_{0.05}(\text{PO}_4)_3$ is the smallest, which indicates its lowest charge transfer resistance. Smaller charge transfer resistance usually results in better high-rate capability. Compared with $\text{Li}_3\text{V}_2(\text{PO}_4)_3$, the smaller particle size and larger lattice volume of $\text{Li}_3\text{V}_{1.9}\text{Ti}_{0.05}\text{Fe}_{0.05}(\text{PO}_4)_3$ contribute to its smaller charge transfer resistance. However, $\text{Li}_3\text{V}_{1.9}\text{Ti}_{0.05}\text{Mn}_{0.05}(\text{PO}_4)_3$ has the largest depressed semicircle and thus the highest charge transfer resistance, which is due to the detrimental effect induced by Mn^{2+} incorporation.

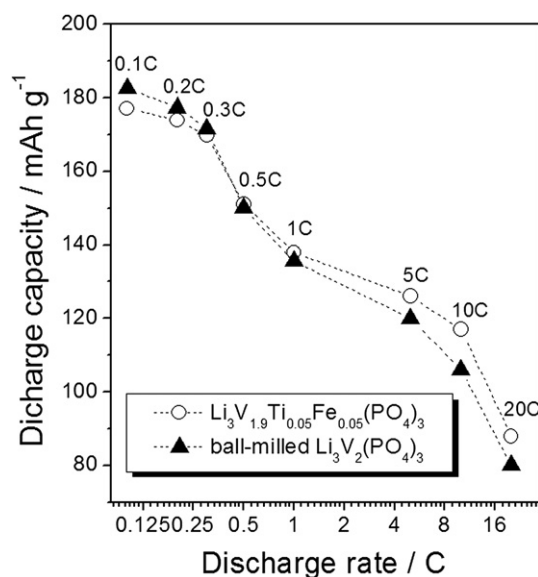


Fig. 14. Rate capability of the ball-milled $\text{Li}_3\text{V}_2(\text{PO}_4)_3$ together with that of $\text{Li}_3\text{V}_{1.9}\text{Ti}_{0.05}\text{Fe}_{0.05}(\text{PO}_4)_3$.

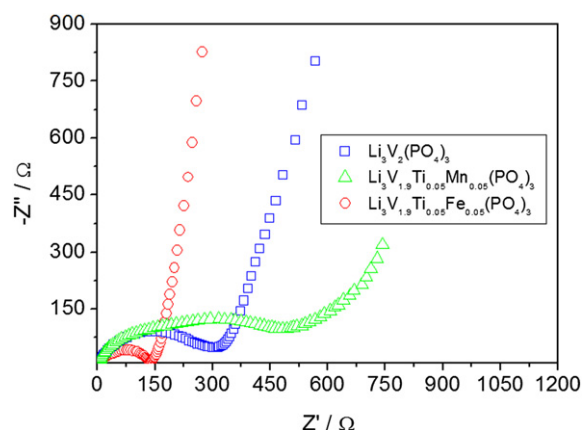


Fig. 15. Nyquist plots of $\text{Li}_3\text{V}_{1.9}\text{Ti}_{0.05}\text{Mn}_{0.05}(\text{PO}_4)_3$, $\text{Li}_3\text{V}_{1.9}\text{Ti}_{0.05}\text{Fe}_{0.05}(\text{PO}_4)_3$ and $\text{Li}_3\text{V}_2(\text{PO}_4)_3$.

4. Conclusions

A citric acid assisted sol–gel method is employed to prepare the Ti–Mn and Ti–Fe codoped $\text{Li}_3\text{V}_2(\text{PO}_4)_3$ samples, i.e. $\text{Li}_3\text{V}_{2-2x}\text{Ti}_x\text{Mn}_x(\text{PO}_4)_3$ and $\text{Li}_3\text{V}_{2-2x}\text{Ti}_x\text{Fe}_x(\text{PO}_4)_3$ ($x = 0, 0.05, 0.1, 0.15, 0.2$ and 0.25). Single phase sample is obtained only if x is equal to 0 or 0.05. Higher value of x , i.e. 0.1, 0.15, 0.2 or 0.25, results in the formation of impurities. The impurities are LiMnPO_4 and $\text{Mn}_2\text{P}_2\text{O}_7$ for the Ti and Mn codoped samples, and the impurity is LiFePO_4 for the Ti and Fe codoped samples. The first charge/discharge capacity of $\text{Li}_3\text{V}_{2-2x}\text{Ti}_x\text{Mn}_x(\text{PO}_4)_3$ and $\text{Li}_3\text{V}_{2-2x}\text{Ti}_x\text{Fe}_x(\text{PO}_4)_3$ decrease with x . Among the three single phase samples, $\text{Li}_3\text{V}_{1.9}\text{Ti}_{0.05}\text{Fe}_{0.05}(\text{PO}_4)_3$ has the best high-rate capability and cycle performance, while $\text{Li}_3\text{V}_{1.9}\text{Ti}_{0.05}\text{Mn}_{0.05}(\text{PO}_4)_3$ has the worst. Compared with $\text{Li}_3\text{V}_2(\text{PO}_4)_3$, $\text{Li}_3\text{V}_{1.9}\text{Ti}_{0.05}\text{Fe}_{0.05}(\text{PO}_4)_3$ have smaller particle size, larger lattice parameter, higher structural stability and lower charge transfer resistance, but the detrimental effect of Mn^{2+} incorporation lead to lower structural stability and higher charge transfer resistance of $\text{Li}_3\text{V}_{1.9}\text{Ti}_{0.05}\text{Mn}_{0.05}(\text{PO}_4)_3$.

Acknowledgment

This work is supported by the National Natural Science Foundation of China (No. 21001036, 50902041), Foundation for University Key Teachers by Heilongjiang Ministry of Education (No. 1155G28), Innovation Foundation of Harbin City (No. 2009RFQXG201) and Program for Scientific and Technological Innovation Team Construction in Universities of Heilongjiang (No. 2011TD010).

References

- [1] A.K. Padhi, N.S. Nanjundaswamy, J.B. Goodenough, J. Electrochem. Soc. 144 (1997) 1188–1194.
- [2] G.R. Gardiner, M.S. Islam, Chem. Mater. 22 (2010) 1242–1248.
- [3] M.S. Islam, R. Dominko, C. Masquelier, C. Sirisopanaporn, A.R. Armstrong, P.G. Bruce, J. Mater. Chem. 21 (2011) 9811–9818.
- [4] S.M. Oh, H.G. Jung, C.S. Yoon, S.T. Myung, Z.H. Chen, K. Amine, Y.K. Sun, J. Power Sources 196 (2011) 6924–6928.
- [5] J. Barker, R.K.B. Gover, P. Burns, A. Bryan, J. Electrochem. Soc. 154 (2007) A307–A313.
- [6] S.C. Yin, P.S. Strobel, H. Grondy, L.F. Nazar, Chem. Mater. 16 (2004) 1456–1465.
- [7] J. Barker, M.Y. Saidi, J.L. Swoyer, J. Electrochem. Soc. 150 (2003) A684–A688.
- [8] D.J. Ai, K.Y. Liu, Z.G. Lu, M.M. Zou, D.Q. Zeng, J. Ma, Electrochim. Acta 56 (2011) 2823–2827.
- [9] M.M. Ren, Z. Zhou, Y.Z. Li, X.P. Gao, J. Yan, J. Power Sources 162 (2006) 1357–1362.
- [10] Y.H. Chen, Y.M. Zhao, X.N. An, J.M. Liu, Y.Z. Dong, L. Chen, Electrochim. Acta 54 (2009) 5844–5850.
- [11] C.S. Dai, Z.Y. Chen, H.Z. Jin, X.G. Hu, J. Power Sources 195 (2010) 5775–5779.

- [12] Q. Kuang, Y.M. Zhao, X.N. An, J.M. Liu, Y.Z. Dong, L. Chen, *Electrochim. Acta* 55 (2010) 1575–1581.
- [13] S.Q. Liu, S.C. Li, K.L. Huang, Z.H. Chen, *Acta Phys. Chim. Sin.* 23 (2007) 537–542.
- [14] M. Sato, H. Ohkawa, K. Yoshida, M. Saito, K. Uematsu, K. Toda, *Solid State Ionics* 135 (2000) 137–142.
- [15] J. Zhai, M.S. Zhao, D.D. Wang, *Trans. Nonferrous Met. Soc. China* 21 (2011) 523–528.
- [16] Y.G. Mateyshina, N.F. Uvarov, *J. Power Sources* 196 (2011) 1494–1497.
- [17] C. Deng, S. Zhang, S.Y. Yang, Y. Gao, B. Wu, L. Ma, B.L. Fu, Q. Wu, F.L. Liu, *J. Phys. Chem. C* 115 (2011) 15048–15056.
- [18] C. Deng, S. Zhang, S.Y. Yang, B.L. Fu, L. Ma, *J. Power Sources* 196 (2011) 386–392.
- [19] C.S. Sun, Z. Zhou, Z.G. Xu, D.G. Wang, J.P. Wei, X.K. Bian, J. Yan, *J. Power Sources* 193 (2009) 841–845.
- [20] I. Milosev, T. Kosec, H.H. Strehblow, *Electrochim. Acta* 53 (2008) 3547–3558.
- [21] J.W. Lee, M.S. Park, B. Anass, J.H. Park, M.S. Paik, S.G. Doo, *Electrochim. Acta* 55 (2010) 4162–4169.
- [22] M.C. Biesinger, B.P. Payne, A.P. Grosvenor, L.W.M. Lau, A.R. Gerson, R.S.C. Smart, *Appl. Surf. Sci.* 257 (2011) 2717–2730.
- [23] R.D. Shannon, *Acta Crystallogr. A* 32 (1976) 751–767.
- [24] L. Wang, Z.C. Li, H.J. Xu, K. Zhang, *J. Phys. Chem. C* 112 (2008) 308–312.
- [25] S.-C. Yin, H. Grondy, P. Strobel, M. Anne, L.F. Nazar, *J. Am. Chem. Soc.* 125 (2003) 10402–10411.
- [26] S. Patoux, C. Wurm, M. Morcrette, G. Rousse, C. Masquelier, *J. Power Sources* 119–121 (2003) 278–284.
- [27] A.R. Cho, J.N. Son, V. Aravindan, H. Kim, K.S. Kang, W.S. Yoon, W.S. Kim, Y.S. Lee, *J. Mater. Chem.* 22 (2012) 6556–6560.
- [28] W.J. Zhang, *J. Power Sources* 196 (2011) 2962–2970.
- [29] J.F. Ni, Y. Kawabe, M. Morishita, M. Warada, T. Sakai, *J. Power Sources* 195 (2011) 2877–2882.
- [30] G. Amatucci, J.M. Tarascon, *J. Electrochem. Soc.* 149 (2002) K31–K46.